Molecular basis of the exciton-phonon interactions in the PE545 light-harvesting complex

Lucas Viani,[1*] Marina Corbella,[2] Carles Curutchet,[2*] Edward J. O'Reilly,[3] Alexandra Olaya-Castro,[3] Benedetta Mennucci[1*]

[1]Dipartimento di Chimica e Chimica Industriale, Università di Pisa, via Risorgimento 35, 56126 Pisa, Italy.

[2]Departament de Fisicoquímica, Facultat de Farmàcia, Universitat de Barcelona, Av. Joan XXIII s/n, 08028 Barcelona, Spain.

[3]Department of Physics and Astronomy, University College London, Gower Street, London WC1E 6BT, United Kingdom

ABSTRACT: Long-lived quantum coherences observed in several photosynthetic pigment-protein complexes at low and at room temperatures have generated a heated debate over the impact that the coupling of electronic excitations to molecular vibrations of the relevant actors (pigments, protein and solvent) has on the excitation energy transfer process. In this work, we use a combined MD and QM/MMPol strategy to investigate the exciton-phonon interactions in the PE545 light-harvesting complex by computing the spectral densities for each pigment and analyzing their consequences in the exciton dynamics. Insights on the origin of relevant peaks, as well as their differences among individual pigments, are provided by correlating them to normal modes obtained from a quasi-harmonic analysis of the motions sampled by the pigments in the complex. Our results indicate that both the protein and the solvent significantly modulate the intramolecular vibrations of the pigments thus playing an important role in promoting or suppressing certain exciton-phonon interactions. We also find that these low-frequency features are largely smoothed out when the spectral density is averaged over the complex, something difficult to avoid in experiments that underscores the need to combine theory and experiment to understand the origin of quantum coherence in photosynthetic light-harvesting.

INTRODUCTION

Photosynthesis is one of the most important processes sustaining life on earth. The understanding of its molecular mechanisms has always been the center of interest in scientific studies, especially due to its high photon-to-charge conversion efficiency or quantum yield at low light conditions, and the possibility of applying similar concepts to artificial light-harvesting and photo-conversion devices. Although over the past decades such molecular mechanisms have been elucidated in detail,[1–3] only recently two-dimensional electronic spectroscopy reported long lived exciton coherence in a variety of pigment-protein photosynthetic complexes.[4–6] These experimental results have generated a heated debate concerning the origin of the coherence and its impact on the excitonic energy transfer efficiency and pathways.[7–9] Coherence effects have been observed even at room temperature in the phycoerythrin 545 (PE545) light-harvesting complex,[6] as well as in the Fenna-Matthews-Olson (FMO) complex,[10] which is an intriguing finding, since at first sight one would expect a quick dissipation of any coherent electronic state formed, due to the interactions with the apparent disordered environment, composed by the motions of the protein scaffold and solvent molecules. This simplistic view does not capture the full influence of the environment as it was originally pointed out by Lee, Cheng, and Fleming, who suggested that spatially correlated environmental fluctuations might support the coherent dynamics of electronic excitations.[4,11,12] Studies combining classical molecular dynamics (MD) and quantum-chemical methods, however, indicate that spatial correlations do not translate into significant correlations among the site energies of the pigments in the Fenna-Matthews-Olson (FMO)[12,13] and PE545[11] complexes. Recent theoretical and experimental studies indicate that the structured nature of the exciton-phonon interaction in light-harvesting antennae, and in particular the coupling of electronic excitations to molecular vibrations, that do not relax quickly to thermal equilibrium, is fundamental for effective energy distribution within these systems[14–19] and may play a central role in the picosecond exciton coherence beating observed in the experiments.[20–22] The coupling to vibrations in ranges that commensurate the energy difference between exciton states may even allow these systems to take on states that are truly quantum coherent with no classical analogue.[23]

It is then clear that a full understanding of the origin and role of coherence in the photosynthetic light-harvesting process can only be achieved via a combination of experimental and theoretical studies. From the theoretical point of view, the study of non-equilibrium energy transfer dynamics in a dissipative medium can be done using the density matrix formalism, which requires a detailed knowledge of the spectral density quantifying the exciton-phonon interaction.[14] Spectral densities can, in principle, be obtained using experimental techniques, such as spectral hole-burning or fluorescence line-narrowing spectroscopy,[24–27] or can be phenomenologically obtained via fitting spectroscopy results.[28] However, in multichromophoric systems often several low-energy chromophores contribute to the fluorescense of the complex, and in this case an averaged spectral density can only be estimated,[14,15] thus missing the information related to the pigments' local environment. Alternatively, several groups have combined MD simulations with quantum chemical calculations[8,9,13,29–34] or electrostatic

calculations coupled to normal mode analysis[35] to theoretically derive spectral densities.

In this work we use hybrid quantum mechanics (QM)/ polarizable Molecular Mechanics calculations combined to classical molecular dynamics (MD) to investigate exciton-phonon coupling in the PE545 antenna of the marine cryptophyte alga *Rhodomonas* sp. strain CS24.[6,28,36–42] PE545 belongs to the family of the light-harvesting antenna proteins classified as phycoerythrins (PE), which are present in Cryptophyte microalgae, ubiquitous members of freshwater and marine environments. These proteins are capable of absorbing the blue-green wavelengths of light that are available after broadband sunlight has passed through water. As in such environments the red wavelengths absorbed by chlorophyll are greatly attenuated, these proteins use tetrapyrrole pigments, called bilins, as the primary antennas.

Recently, PE545 has been studied both experimentally[6,28,36,38,39,42] and computationally[11,14,37,40,43] due to its capability to photosynthesize in low-light conditions, suggesting an efficient absorption of incident sunlight. This high efficiency is partially due to the flexible structural nature of the pigments which allows the modulation of their absorption energy through local pigment–protein interactions.[40] This feature maximizes the absorption of incident photons while creating an excitation funnel that drives the excitons formed inside of the complex to its exterior, facilitating its transfer to another complex or to the reaction center.[40] To understand the role of vibrations of the pigment-protein complex, eventually coupled to the solvent, we have computed the spectral density of the individual pigments and performed an analysis of the nuclear degrees of freedom of the pigments, the protein scaffold and the solvent to give insights into the intra- and intermolecular origin of the features characterizing the frequency dependent coupling among the electronic system and its environment. To get such a picture we have confronted quasi-harmonic (QH) and normal mode analysis (NMA). While NMA proves the vibrations around a single minimum, QH analysis aims at characterizing the global extent of the configurational space accessible to the system along an MD simulation. The modes obtained from the QH analysis can then be directly connected to the fluctuations of the energies experienced by the pigments along the MD trajectory.

Our results indicate that the protein and solvent significantly impact the distribution of motions sampled by the PE545 pigments, thus altering the structure of the individual spectral density experienced by each bilin, specially at low (<500 cm^{-1}) and mid-frequency ranges (500-800 cm^{-1}). Because recent reports[40] indicate that several excitonic differences in PE545 will commensurate with the energies in this frequency range, accounting for such individual features on the pigments spectral densities will be important to clarify the origin of quantum coherence. We also find that these low and mid-frequency features are largely smoothed out when the spectral density is averaged over the complex, something difficult to avoid in experiments that underscores the need to combine theory and experiment to understand the origin of quantum coherence in photosynthetic light-harvesting. We finally consider subunits within the antennae complex to illustrate some implications of pigment-dependent spectral densities and how averaging over the spectral densities may hide important features of the spatio-temporal distribution of energy within the complex. Our results open the door for future studies where the full implications of billin-dependent spectral densities in ultrafast spectroscopy and full exciton dynamics can be thoroughly analysed.

METHODOLOGY

2.1 Spectral densities

The spectral density, $J_i\ (\omega)$, describes the frequency-dependent system-bath coupling strength of the pigment *i*. As it has been recently clarified, the spectral density can be expressed as[33,44,45]

$$J_i\ (\omega) = \frac{\beta\omega}{\pi}\int_0^\infty C_i^{cl}\,(t)cos(\omega t)dt \qquad (1)$$

where $\beta = 1/(K_B T)$ and $C_i^{cl}(t)$ is the classical autocorrelation function of the fluctuation of the site energies:

$$C_i^{cl}(t_j) = \frac{1}{N-j}\sum_{k=1}^{N-j} \Delta E_i(t_j + t_k)\Delta E_i(t_k) \qquad (2)$$

$C_i^{cl}(t)$ is here obtained using a methodology combining classical MD simulations and QM calculations of the site energies. In particular, a polarizable quantum mechanical/molecular mechanical (QM/MMPol) methodology we recently developed[46] has been used and applied to the configurations extracted from classical MD simulations. In this work we have used the same set of data generated in ref.[11], where we performed a 300 ps (after 10 ns equilibration) MD simulation of PE545 in water at 300 K (see Ref. [40] for details), from which snapshots were extracted every 5 fs, thus totalizing 60000 frames. In a next step, QM/MMPol calculations of site energies were performed for each pigment along the classical trajectory, allowing the calculation of the autocorrelation function of their fluctuations. Due to the large number of calculations to be performed (480000) and their computational cost, we adopted the ZINDO semiempirical method with the Zerner's spectroscopic parameterization[47] to describe the excited states of the pigments, whereas the protein and solvent environment were described using a polarizable force field we developed from DFT calculations[40] (more details about the computational strategy are reported in Refs.[11,40,43]). All PEBs and DBVs were modeled having unprotonated propionate chains as well as fully protonated central pyrrole rings, leading to a total -1 charge. Crystallograhic data and the conservation of the Asp residue coordinating the central rings strongly suggest this protonation pattern for PEBs.[39] For DBVs, the crystal data is less conclusive, but it also indicates a neutral His residue coordinating the DBVs thus suggesting also this protonation pattern.

The autocorrelation functions were computed from the discrete time series following Equation 2, using fluctuations of the site energies, $\Delta E_i(t_k)$,[29] computed every 5 fs of the MD trajectory. In the PE545 complex, the fastest oscillations in the energies were found to have a period around 20 fs similar to what has been found for the FMO complex, this time step thus provides a good compromise between reducing the amount of calculations without losing track of their oscillations at ambient temperature.[13] Multiple autocorrelation functions of 2 ps length were computed using the 300 ps window by shifting its initial time by 1 ps. The final function was then obtained as the average of all functions computed for the same pigment. To minimize the effects of the noise in the spectral densities the final autocorrelations were multiplied by a Gaussian envelop of variance $\sigma^2 = 3.6 \times 10^5$ fs^2 ensuring their convergence to zero.[45] The final autocorrelation functions are shown in Figure 2. The high-frequency offset in the spectral densities was corrected with negligible effects in the low-frequency part by shifting the Fourier transform before its multiplying by the prefactor.[48] The spectral densities obtained from Equation (1) were finally fitted

using an expression composed of two terms, one describing coupling to a continuous distribution of modes and a second one associated to discrete vibrational modes:

$$J(\omega) = J_{continuous}(\omega) + J_{peaks}(\omega) = \frac{2\lambda}{\pi}\frac{\Omega\omega}{\omega^2+\Omega^2} + \sum_q \frac{2\lambda_q}{\pi}\frac{\nu_q\omega_q^2\omega}{\left(\omega_q^2-\omega^2\right)^2+\nu_q^2\omega^2} \quad (3)$$

$J_{peaks}(\omega)$ corresponds to the spectral densities of a set of damped quantum harmonic oscillators of frequencies ω_q with associated damping υ_q and reorganization energy $\lambda_q = s_q\omega_q$, whereas the continuous contribution has associated a reorganization energy λ and a bath cutoff frequency Ω.

2.2 Quasi-harmonic and normal mode analysis

The peaks in the spectral densities correspond to motions of the system coupled to the electronic transitions of the pigments. In order to identify the molecular origin of these motions, we performed a quasi-harmonic (QH) analysis of the motions of each pigment in PE545 along the classical MD trajectory.[49] Such analysis requires diagonalization of the mass-weighted covariance matrix of atomic positions in Cartesian coordinates, and is typically used to determine configurational entropies of biomolecules. The corresponding eigenvectors describe motional modes (quasi-harmonic modes) around the average system configuration. To characterize the peaks on the spectral density of each individual pigment, a separate QH analysis was performed on the coordinates of the atoms of each pigment. Translational and rotational motions were removed from the analysis by superimposing each snapshot to the average pigment structure sampled along the 300 ps MD trajectory.

In order to assess the accuracy of the classical force field adopted in our simulation in describing the intrinsic vibrations of the pigments, we have also performed an NMA analysis of each pigment both at classical MM and QM levels. Classical MM-NMA analysis was performed using the same force field adopted in the MD simulation, whereas the QM-NMA analysis was performed at the B3LYP/6-31G(d) level of theory. In this latter case, we scaled the resulting vibrational frequencies by 0.952 in order to reproduce fundamental frequencies according to the Minnesota Database of Frequency Scale Factors for Electronic Model Chemistries.[50] Both in MM and QM NMA analysis, the geometry of the pigments was minimized. In such a minimization, the cysteine links connecting the pigments with the protein were substituted by -SCH_3 groups. Finally, we note that in the QM-NMA analysis, the propionic acid groups in the bilin pigments were protonated to prevent folding and keep the biological conformation.

RESULTS AND DISCUSSION

The crystal structure of PE545, illustrated in Figure 1, has been determined at 1.63 Å[41] and later at 0.97 Å resolution.[39] It is organized as an $\alpha_1\alpha_2\beta\beta$ dimer, and contains eight bilins, characterized by a linear tetrapyrrole structure covalently linked to the protein scaffold. In particular, three types of bilins can be singled out: two 15,16-dihydrobiliverdin chromophores, labeled DBV_A and DBV_B, singly bounded to the α subunit A and B, four phycoerythrobilin chromophores, labeled PEB_{158C}, PEB_{158D}, PEB_{82C}, and PEB_{82D}, singly bounded to the subunit β C or D, and two other phycoerythrobilin chromophores, labeled $PEB_{50/61C}$ and $PEB_{50/61D}$, doubly bound to the same subunits C and D, respectively. The overall PE545 structure (and the chromophores) displays a pseudosymmetry about the 2-fold axis relating the $\alpha_1\beta$ and $\alpha_2\beta$ monomers.

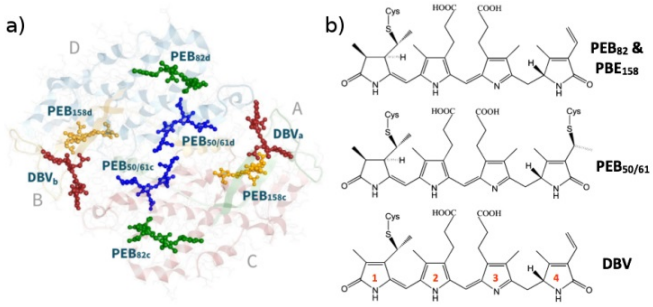

Figure 1: (a) Structure of the $\alpha_1\alpha_2\beta\beta$ dimer structure of the PE545 complex (α chains are in red and blue whereas the polypeptide β chains are in orange and cyan) and relative position of the eight light-absorbing pigments; (b) structural view of the two types of bilins: dihydrobiliverdins (DBV) and phycoerythrobilins (PEB) (the ring numbering used in the text is also shown). The 3D molecular representations was created using the MView software.[51]

In a recent study,[40] we have shown that, in contrast to chlorophyll-based photosynthetic complexes, pigment composition and conformation play a major role in defining the energy ladder in the PE545 complex, rather than specific pigment-protein interactions. This is explained by the remarkable conformational flexibility of the eight bilin pigments in PE545, characterized by a quasi-linear arrangement of the four pyrrole units. Such conformational degrees of freedom are therefore expected to significantly couple with motions in the protein-solvent environment and give rise to strong peaks in the spectral density of the various pigments. In the following sections this investigation is reported and further supported by a detailed molecular explanation of the main features observed in the spectral densities.

3.1 Spectral densities

The autocorrelation functions computed from the site energies extracted from the MD trajectories are reported in Figure 2. The convergence of the autocorrelations were tested against the number of frames, and no significant changes were observed for data sets larger than 25000 frames.

As a general comment, we can see that the fluctuations of the autocorrelation functions of all the bilins are larger than those previously found for the bacteriochlorphylls in the FMO complex[13] and the autocorrelation functions, particularly for the DBV bilins, decay much slower than those of the average FMO pigments. Once observed that, it is also worth noting that different features among pigments are evident. In particular, DBVs present much larger oscillations with respect to all the other pigments. This is a consequence of the additional double bond present in DBVs, which translates into a more delocalized π- π* electronic transition involving not only pyrrole rings 2 and 3 as in PEBs, but also ring 1 (see Fig. 1). This increased conjugation thus leads to an excited state more sensitive to structural deformations, as will be discussed later.

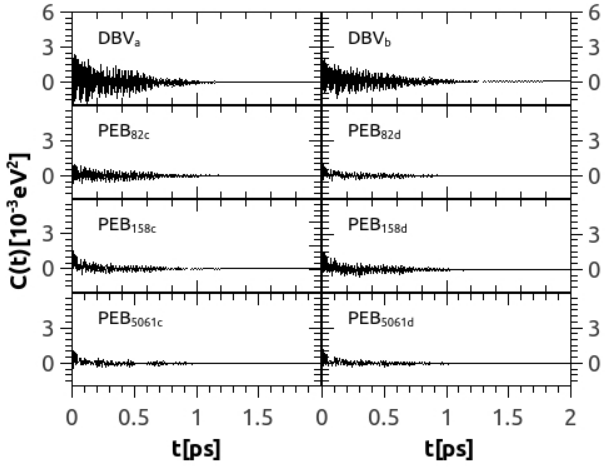

Figure 2: Site energy autocorrelation functions for the eight bilins in the PE545 complex.

In Figure 3 we report the resulting spectral densities averaged over all pigments (top) and over the pseudo-symmetric pairs (bottom). The spectral density averaged over all pigments is confronted against that reported in ref.[14], based on linear spectra and spectroscopy studies,[28,39] and we observe a reasonable agreement between the curves at low frequencies, representing the continuous component of the spectral density. Regarding the discrete peaks of the spectra, we obtained also reasonable peak intensities and amplitudes, although different frequency positions are predicted. High-frequency modes tend to be overpopulated in classical simulations, so the high-frequency part of the spectral density is expected to be less reliable compared to the low frequency region. The experimental spectral density, however, can also be affected by the way spectroscopic data was fitted, so the position of the peaks in this case must be taken with caution. Nevertheless, we computed the reorganization energies associated to each spectral density through the relation $\lambda = \int_0^\infty \frac{J(\omega)}{\omega} d\omega$ and we find an excellent agreement between our predicted estimate (557 cm^{-1}) and the value derived from the experimental spectral density (539 cm^{-1}).

As a general feature we see that the spectral densities are highly structured and the most recently reported electronic energies[40] indicate that several of the excitonic energy differences will commensurate with the energies at which the sharp peaks are observed with significant implications for the excitation dynamics as recently discussed.[14] In addition to this general behavior, we also note that there are distinctive differences among the spectra of each of the bilins throughout the whole frequency regime. These differences are easily observed among non-symmetric pairs and indicate different local environments for the excitation of each bilin. Therefore the assumption of equal spectral densities for all pigments used in different reports to compute spectroscopic properties is an important approximation to the problem,[28,40,52] and its impact in the excitonic dynamics is discussed in detail in section 3.3. A major difference of the spectral densities for DBVs and PEBs comes from the effective coupling to the continuous distribution of harmonic modes in the low-frequency regime, which is reflected in the different values of the effective reorganization energies of this continuous component. The DBVs feature larger reorganization energies (λ is around 82 cm^{-1}) when compared to PEBs. Among the PEBs, the largest system-bath coupling appears to be for the PEB$_{158}$ pair followed by the PEB$_{50/61}$ and PEB$_{82}$ pairs featuring λ values of ~48, ~37, and ~20 cm^{-1} respectively. Such changes in λ are expected to manifest themselves in differences in the picosecond exciton dynamics as discussed below.

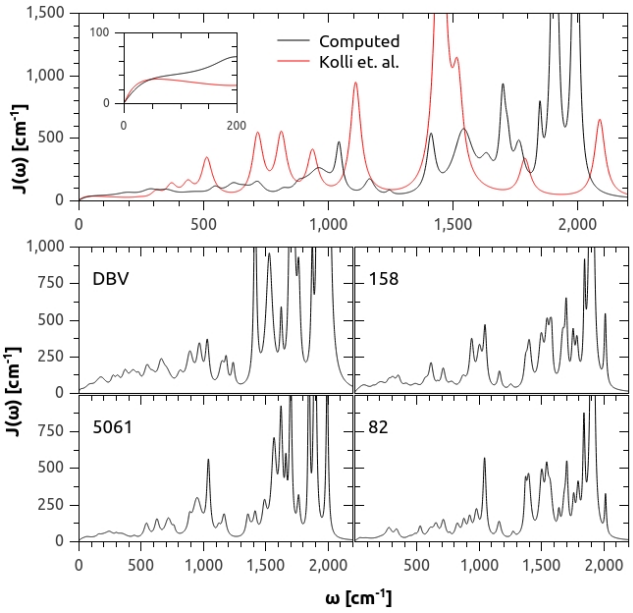

Figure 3: Averaged ambient temperature spectral densities averaged over all pigments confronted against the experimental one reported in Novoredezky [28] and used by Kolli et.al.[14] (top), and spectral densities averaged over pseudo-symmetric bilins (bottom) in the PE545 complex. The corresponding pigment number is shown on the top-left corner of the plot. The inset shows a close-up of the low frequency region.

3.2 Origins of the peaks

To understand the differences in the peaks featured in the spectral densities of each pigment, it is important to determine the molecular nature of such vibrations. To this aim, we have determined the motions sampled by each pigment using both a normal mode (NMA) and a Quasi-Harmonic (QH) analysis based on the MD simulations. Before performing this analysis, the quality of the classical force field used to describe the bilin motions was checked by comparing the distributions of modes obtained from the NMA analysis to those obtained at DFT- B3LYP level.

Such a comparison is reported in Figure S3. Overall, the distributions obtained with QM and classical methods are in reasonable agreement, although a slight shift at the high-frequency region (1500-1700 cm^{-1}) is observed which can be related to the fact that in the QM analysis, the propionic acid groups in the bilin pigments were protonated to prevent folding and keep the biological conformation. In addition, the MM distribution has a larger number of modes at very low frequencies (< 50 cm^{-1}). Although this analysis only provides a partial verification of the MM force field, as individual modes can be

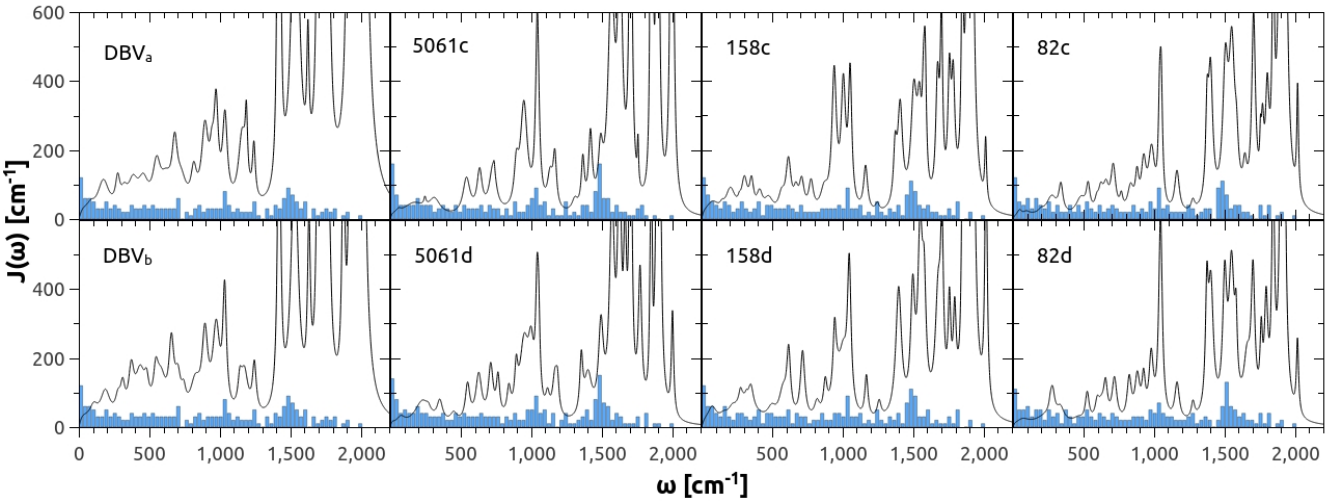

Figure 4: Ambient temperature spectral densities of the eight bilins in the PE545 complex (black lines), and the respective distribution of MM normal modes (blue bars). The height of the bars was homogeneously scaled for visualization purposes.

located at slightly shifted frequencies as compared to the QM description, overall it indicates that the distribution of modes is reasonable. The validation of the classical description of the bilin motions against QM results allows us to apply the QH analysis along the trajectory and use the distribution and nature of the quasi-harmonic modes obtained to investigate the features of the spectral density at a molecular level. In Figure 4, we show the distribution of QH modes determined for the individual bilins along with the corresponding spectral densities.

A high density of modes is observed in the regions 850-1200 cm^{-1} and 1400-1700 cm^{-1}, matching the largest peaks in the spectral densities. At frequencies larger than 800 cm^{-1}, all pigments show similar features, pointing to the intramolecular character of the motions, although the coupling strength of the peaks differs among pigments. Interestingly, however, pseudo-symmetric pairs of bilins show very similar coupling strengths, despite the different sequence of the α polypeptide chains in the $\alpha_1\alpha_2\beta\beta$ dimer structure of the PE545 complex, which slightly breaks the symmetry of the system (see Figure 1). Because the vibrations of the pigments are coupled to different environments, the distribution of QH modes can change thus modulating the relative intensities of the peaks. Also in the 500-800 cm^{-1} range, all pigments show somewhat similar peaks. However, in this case the differences in the peak distribution and intensities are enhanced compared to the higher-frequency region. In the low-frequency range (<500 cm^{-1}) instead all pigments exhibit significant differences both in position and coupling strength of the peaks, even among pseudo-symmetric pairs. This suggests that low-frequency motions of the pigments are strongly modulated by their local environment. This can be clearly appreciated in the spectral density averaged among all pigments shown in Figure 3, as the different peaks apparent in the individual pigments are smoothed out. Among the different pigments, clearly the DBVs show the largest couplings to these low-frequency modes. Inspection of the atomic displacements involved in such modes indicates that many of them include bendings of the global linear tetrapyrrole arrangement of the bilins or torsional motions modifying the degree of planarity among the pyrrole rings; such displacements presumably modify the degree of π-conjugation among the rings and therefore are expected to couple significantly to the π - π* transition. Because the DBVs have a further double bond in the pyrrole ring 1 bonded to the Cys residue in the protein (see Figure 1), the electronic excitation in this pigment extends over rings 1, 2 and 3, whereas in PEBs the excitation mainly involves rings 2 and 3. Such low-frequency motions modifying the degree of π-conjugation of ring 1 will couple much more strongly to the DBVs excitations, thus explaining the previously observed high reorganization energy. It is also interesting to note that the PEBs of the central pair, PEB$_{50/61C}$ and PEB$_{50/61D}$, show the smallest coupling to low-frequency motions. In contrast to the other PEBs, these bilins are linked to two Cys residues of the protein through rings 1 and 4, and such links could reduce the ability of the whole linear tetrapyrrole arrangement to bend or to stretch, compared to the other PEBs, thus reducing the coupling of low-frequency motions to the electronic excitation. These observations give an explanation of the previously observed low reorganization energies for these two sets of bilins.

It is important to note that the distribution of QH modes allows us to unveil the molecular basis of the peaks in the spectral density by associating them to modulated bilin intramolecular motions in the protein environment. The actual impact in the spectral density peaks can, however, either arise from fluctuating electrostatic pigment-protein interactions associated to a given motion or from oscillations in the bilin transition energies induced by changes in their internal geometries. It is remarkable that all spectral density peaks correspond to some distribution of normal modes, even the peaks at ~2000 cm^{-1}. On the other hand, not all QH modes are expected to contribute to the spectral density, only those showing a strong exciton-phonon coupling.

The inspection of the atomic displacements involved in the modes thus allows explaining the molecular origin of the peaks. We have done such inspection for the modes in the 500-600 cm^{-1}, 950-1050 cm^{-1} and 1400-1500 cm^{-1} regions, which include the most remarkable peaks found in the overall averaged spectral density shown in Figure 3. In addition, we have analyzed the modes in the 650-750 cm^{-1} range, in order to shed light on the ~710 cm^{-1} peak which is better resolved in PEBs compared to DBVs. For the sake of simplicity, we only focus on the modes that are expected to couple more strongly to the π- π* transition that extends over pyrrole rings 2 and 3 in the PEBs, and 1, 2 and 3 in the DBVs. Such modes involve torsional motions δ(ring) distorting the planarity of the

pyrrole rings, out of plane and in plane bendings of the rings, γ(ring) and β(ring), respectively, and υ(C-C) and υ(C-N) stretchings leading to ring breathings. More in detail, in the 500-600 cm^{-1} range, the interesting modes mostly involve δ(ring), γ(ring) and β(ring) displacements whereas in the 950-1050 cm^{-1} region, the vibrations are characterized by a mixing of β(ring), υ(C-C) and υ(C-N) distortions. Finally, modes in the 1400-1500 cm^{-1} range mostly involve υ(C-C) and υ(C-N) stretchings. Because the DBVs have a further C=C double bond in ring 1, there is a larger number of modes strongly coupled to the DBVs in this region compared to PEBs, which explains why the ~1450 cm^{-1} peak is considerably more intense in the DBVs compared to the PEBs. In Table S1-8. we report the individual rings of each bilin involved in the δ(ring), γ(ring), β(ring), υ(C-C) and υ(C-N) displacements for each mode in these frequency ranges, thus allowing identification of those expected to be strongly coupled to the excitation.

In Figure 5 we show a graphical representation of the displacements involved in modes found at about 550 cm^{-1}, 1050 cm^{-1} and 1450 cm^{-1}, which can be connected with the strongest peaks in the spectral density averaged over the pigments in PE545. In the same Figure, we also provide a comparison of two modes observed around 700 cm^{-1} for a PEB and a DBV, respectively.

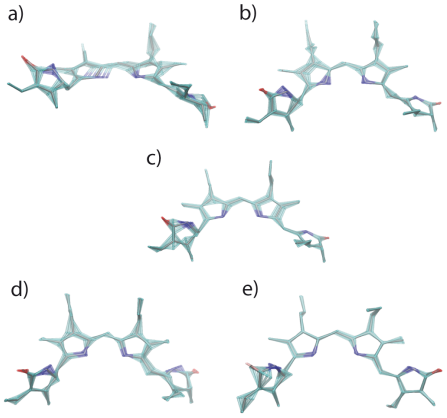

Figure 5: Graphical representation of selected quasi-harmonic modes. a) Mode at 555 cm^{-1} of PEB_{158D}, b) Mode at 1053 cm^{-1} of PEB_{158D}, c) Mode at 1428 cm^{-1} of PEB_{158D}, d) Mode at 711 cm^{-1} of PEB_{158D}, and e) Mode at 697 cm^{-1} of DBV_{19A}.

Close inspection of the two modes around 700 cm^{-1} indicates that, whereas for PEBs distortions of the central pyrrole rings 2 and 3 are evident, for DBVs the mode does not significantly distort rings 1, 2 or 3. This explains why for PEBs such modes show a stronger coupling compared to DBVs.

As previously discussed, the local protein environment translates into slightly different features of the spectral densities found for each pigment, especially at low frequencies. In order to shed light on the modulation of the vibrational modes induced by the protein environment, it is interesting to compare the distribution of vibrational modes obtained either from the QH or the NMA analysis based on the same potential energy function. This comparison is shown in Figure 6.

The results indicate two interesting effects. First, the large accumulation of modes around 1000 and 1500 cm^{-1} found in the NMA distribution is smoothed out when such modes couple to the protein motions, as shown in the QH distribution. On the other hand, there is a slight increase in the number of modes observed in the QH histograms around 500 cm^{-1} compared to its NMA counterparts. These two effects are similar for all pigments, including the $PEB_{50/61C}$ and $PEB_{50/61D}$ bilins linked twice to the protein scaffold, thus suggesting that this effect is not induced by such covalent links but rather by the overall coupling among protein and pigment motions.

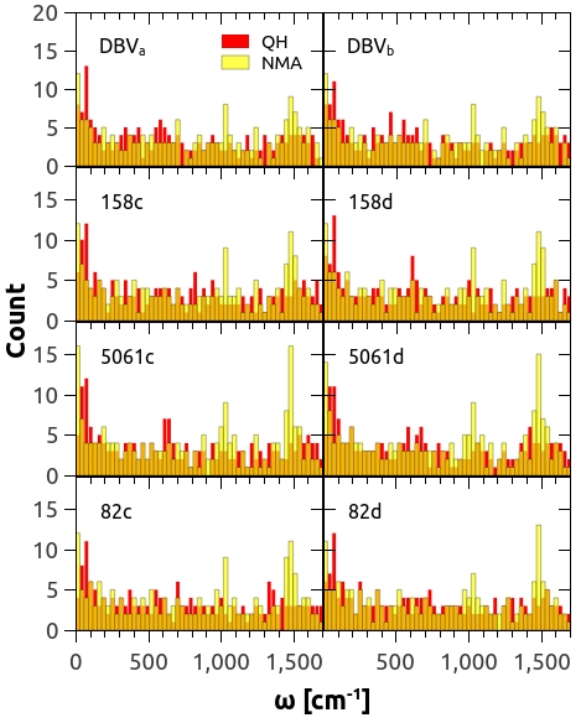

Figure 6: Comparison between quasi-harmonic and normal mode analysis distributions of vibrational frequencies.

To investigate the impact of the solvent on the spectral density, the same quasi-harmonic analysis was repeated for a MD trajectory of the PE545 complex in vacuo (see Ref. [11] for details). A direct comparison between the distributions of normal modes provides an insight on modes that are promoted or suppressed by the presence of the solvent. In Figure 7 it is shown the difference between the distribution of normal mode frequencies in water and gas phase; positive/negative blue/red bars indicate modes that are promoted/suppressed by the solvent, while the bars around zero indicate modes that are not affected by the presence of the solvent. Interestingly, the solvent promotes a large accumulation of modes at particular high frequencies, where the spectral densities feature the larger couplings, whereas in vacuum the modes spread over a larger range of values, indicating the important role of the solvent in modulating the exciton-phonon couplings.

The analysis of the plots suggests that the majority of the peaks in the mid-frequency region (900-1200 cm^{-1}) and high-frequency region (1400-1600 cm^{-1}) present in the spectral densities are strongly promoted by the solvent, i.e. the solvent contributes to accumulate modes at these frequencies. Thus, the protein smoothening of the large accumulation of modes around 1000 and 1500 cm^{-1} suggested by the comparison of NMA and QH mode distributions in Figure 6 seems to be partially counterbalanced by the effect of the solvent. These results thus indicate that the solvent significantly impacts the structure of the spectral density. It is interesting to note that the PEB_{82C} and PEB_{82D} pigments are significantly less

exposed to the solvent than the other chromophores. Also, the central $PEB_{50/61D}$ bilin is more exposed to water compared to $PEB_{50/61C}$ (see also Figure 4 in Ref. [40]). Despite these differences, only PEB_{82D} shows a somewhat smaller impact of the solvent in the distribution of modes compared to the other pigments. This finding suggests that the solvent mostly impacts the bilin vibrations indirectly by modulating the overall protein motions.

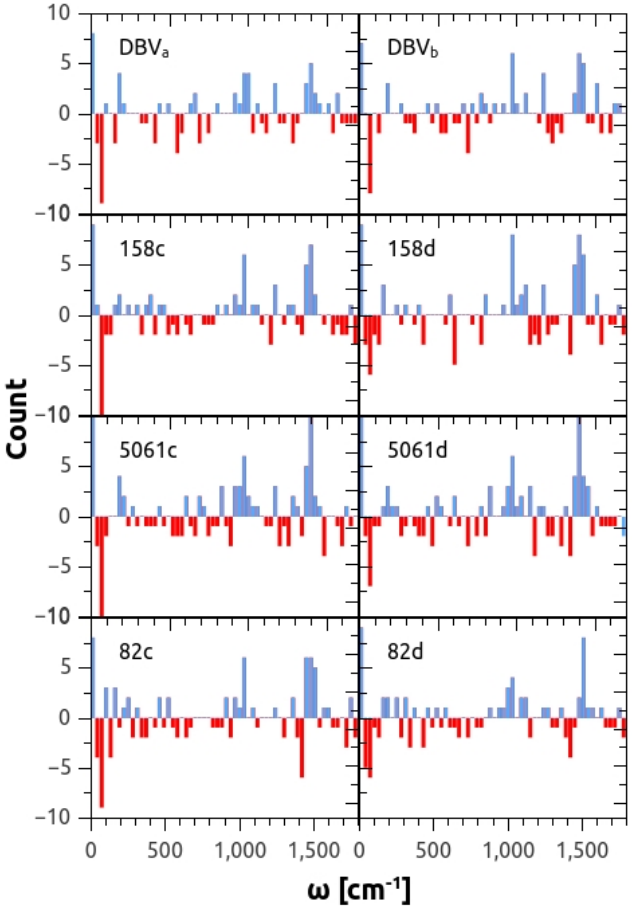

Figure 7: Variation of molecular normal mode distribution in water against the vacuo simulation. Blue/red bars indicate the modes that were promoted/suppressed by the solvent, and its height represents the intensity of the effect.

3.3 Implications for excitation dynamics

The above analyses indicate that the main differences in the spectral densities appear between non-symmetric pairs: the PEBs have reduced reorganization energies in comparison to the DBVs while the latter have spectral densities that are closer to the average fitted via ensemble measurements. In order to illustrate the implications of these billin-dependent spectral densities we consider two sub-sets of chromophores in PE545 and investigate the exciton population dynamics within each sub-set comparing the case when all pigments have identical spectral densities with the case when the spectral densities are different as predicted by our QM/MMPol calculations. On the basis of the site energies reported in Table S4 of Ref.[40], we defined one high-energy sub-set which includes the $PEB_{50/61C}$ and $PEB_{50/61D}$ and a low-energy sub-set which includes PEB_{82C} and PEB_{82D}; in both subsets DBV_a is included as potential trapping site. Using the electronic couplings and site energies reported in Ref.[40], we performed non-perturbative calculations of the exciton dynamics[53,54] considering spectral densities featuring a coupling to a continuous distribution and to a single relevant broaden vibrational mode as presented in Eq. (3). Details of the methodology for computation of exciton dynamics are presented in section 3 of the Supporting information. The results shown in Figures 8 and 9 indicate that averaging spectral densities among non-symmetric pairs results in qualitatively different features of the spatio-temporal distribution of excitation for the high- and low-energy subsets.

Our mode analysis and the corresponding fittings for the spectral densities predict that the three billins in the high-energy sub-unit ($PEB_{50/61C}$, $PEB_{50/61D}$ and DBV_a) exhibit a significant coupling to a mode around $\omega_q = 1050$ cm^{-1} with coupling strength about $\lambda_q = 18$ cm^{-1} and broadening $\nu_q = 31$ cm^{-1}. In this high-energy sub-set, this vibrational mode is quasi-resonant with the energy gap between the intermediate-exciton state (quasi-localised in $PEB_{50/61D}$) and the lowest exciton (quasilocalised in the DBV_a) and then it dominates transfer to this exit site. As already discussed, the PEBs feature a reorganization energy of $\lambda = 36$ cm^{-1} with cut off frequency $\Omega = 32$ cm^{-1}, which is smaller than the parameters for the continuous spectral density for DBV_a which are $\lambda = 80$ cm^{-1} and $\Omega = 42$ cm^{-1}. Considering that initially only the highest exciton state is excited, we observe that non-equilibrium vibrational dynamics is manifested in population oscillations of the intermediate exciton state (quasilocalised in $PEB_{50/61D}$) that lasts up to few hundred of femtoseconds, while the smaller reorganization energy leads to an overall slower transfer to the intermediate and lower exciton states as illustrated in Figure 8 (top). Inset in Fig. 8 depicts the femtosecond coherent (oscillatory) population of the intermediate state, which arises from coupling to the underdamped mode that is comparable with the electronic coupling between the $PEB_{50/61D}$ and DBV_a (see parameters listed in Eq. S3 of the SI). Such coherent energy transfer is washed away when all the sites are considered to have the same continuous component of the spectral density as the DBV_a.

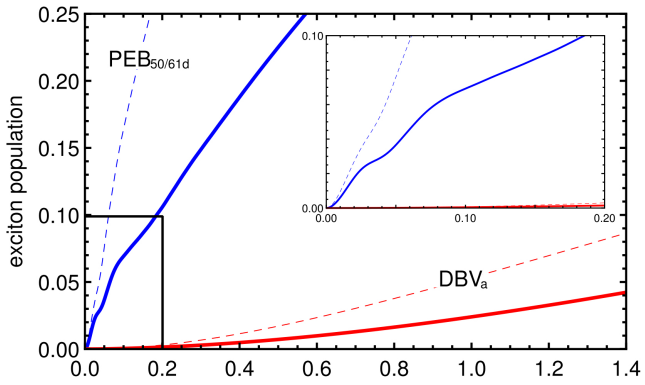

Figure 8: Population dynamics for the intermediate (blue lines) and lowest (red lines) exciton states of the high-energy subunit that includes the PEB50/61C, PEB50/61D and DBVa bilins. Solid lines denote the dynamics with different spectral densities for the three pigments while dashed lines denote the situation with identical spectral densities.

For the low-energy sub-set, our analysis indicate that the PEB_{82C}, PEB_{82D} are coupled to a vibrational mode of frequency around $\omega_q = 530$ cm^{-1} with a strength of $\lambda_q = 8$ cm^{-1} and a broadening $\nu_q = 33$ cm^{-1} while the DBV_a is coupled to a mode of energy $\omega_q = 553$ cm^{-1} with λ_q

= 22 cm^{-1} and ν_q = 65 cm^{-1}. A vibrational mode of this energy is quasi-resonant with the energy gap between the highest and intermediate energy exciton states (quasi-localised in PEB_{82C} and PEB_{82D}, respectively), and therefore is expected to influence exciton transport in this sub-unit. Moreover, the PEB_{82} bilins exhibit weak coupling to a continuous component with λ = 20 cm^{-1} and Ω = 31 cm^{-1}, while the DBV_a is coupled to continuous spectral density with which is λ = 80 cm^{-1} and Ω = 42 cm^{-1} as before. Starting with an excitation in the highest exciton state, Figure 9 depicts the populations of the intermediate and lowest exciton states of this sub-unit when spectral densities are different (solid lines) and identical to the DBV_a (dashed lines). The main effect of the reduced reorganisation energies for the PEBs is a decrease of the rate of transfer to both exciton states. Since the coupling to the localised vibrational mode is weak, its non-equilibrium dynamics only induces some non-exponential growth of population of the intermediate exciton state in the 200 fs time scale as clearly seen in the inset. Both the oscillatory and non-exponential growth of exciton population for intermediate states shown in Figure 8(inset) and Figure 9(inset) indicate that energy dissipation into the thermal background is transiently prevented as has been recently discussed [22], and therefore coherent energy transport is at play in this time scale.

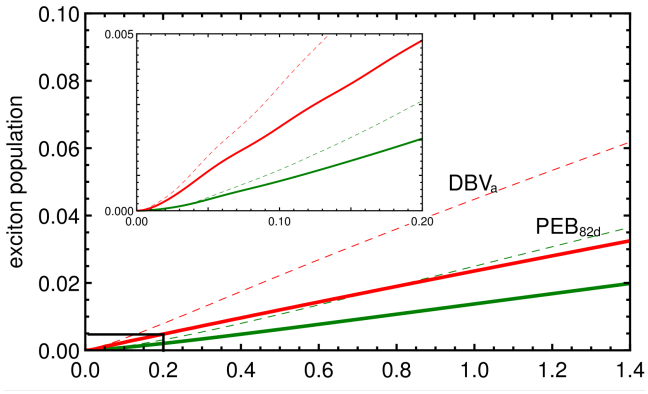

Figure 9: Population dynamics for the intermediate (green lines) and lowest (red lines) exciton states of the low-energy subunit that includes the PEB82C, PEB82D and DBVa bilins. Solid lines denote the dynamics with different spectral densities for the three pigments while dashed lines denote the situation with identical spectral densities.

From the experimental viewpoint, we expect that transient absorption could witness the influence of billin-dependent spectral density in the dynamics. While the spectral density that has been experimentally fitted gives a good agreement with the fluorescence spectra of PE545, the agreement is not as good in the case of the transient absorption. It is also important to highlight that the fitted spectral density in Ref. 27 was made in the framework of modified Redfield that is known to overestimate rates of transfer. These two points justify once more the need for atomic-level and alternative determination of spectral densities. A complete study of the implications of billin-dependent spectral densities for transient spectra and full exciton dynamics is out of the scope of this paper and will be presented in a separate publication.

CONCLUSIONS

In this work we have combined a recently developed QM/MMPol formulation with MD techniques to compute the spectral densities characterising exciton-phonon interactions in the PE545 light-harvesting complex. We have shown the existence of drastic differences in the spectral densities of individual pigments of the PE545 when compared to those averaged over pseudo-symmetric pairs or over all pigments. We predicted some implications of such differences in the population dynamics for the intermediate and lowest exciton states of the pigments, concluding that using averaged spectral densities one cannot predict accurately the effects of non-equilibrium vibrational dynamics in the excitation energy transfer. We expect that such differences could be seen in transient absorption experiments and will in general lead to a richer dynamics of the coherences among exciton states though a complete study in this direction is out of the scope of this paper.

We have analysed the rich structure of the individual spectral densities as a function of energy and identified the prominent peaks that indicate preferential coupling to specific vibrational modes. The origin of such peaks were investigated and correlated to intramolecular normal modes using the quasi-harmonic and normal mode analyses. Equally, the impact of the solvent was analysed, leading to unexpected findings suggesting that it modulates the coupling of the lowest excited state to the environment by promoting or suppressing certain normal modes using the protein scaffold as a pathway.

The identification of the structural origins of the exciton-phonon interactions driving exciton transfer in photosynthetic systems as given in this study provides important guidelines for the design of new experiments that probe and exploit the largely unexplored correlated exciton-vibrational dynamics in light-harvesting complexes.

SUPPORTING INFORMATION

Details of the methodology for the computation of exciton dynamics, tables reporting the individual rings of each bilin involved in the displacements of the QH modes, and figures comparing the distributions of modes obtained from the NMA analysis to those obtained at DFT-B3LYP level.

Acknowledgements

The European Research Council (ERC) through the Starting Grant proposal n. 277755 (EnLight) is acknowledged by B.M. and L.V.. C.C. and M.C. acknowledge support from the Ministerio de Economía y Competitividad of Spain (grants CTQ2012-36195, RYC2011-08918 and BES-2013-064088) and computational resources provided by the Centre de Supercomputació de Catalunya. A.O-C and E.J.O thank the Engineering and Physical Sciences Research Council of the UK (EPSRC) Grant EP/G005222/1 and the EU FP7 Project PAPETS for financial support (Grant Agreement n. 323901).

Corresponding authors:
lucas.viani@for.unipi.it, carles.curutchet@ub.edu,
benedetta.mennucci@unipi.it

References

1. R. J. Cogdell, A. Gall, and J. Köhler, *Q. Rev. Biophys.*, 2006, **39**, 227–324.

2. Y.-C. Cheng and G. R. Fleming, *Annu. Rev. Phys. Chem.*, 2009, **60**, 241–62.

3. V. Sundström, *Annu. Rev. Phys. Chem.*, 2008, **59**, 53–77.

4. H. Lee, Y.-C. Cheng, and G. R. Fleming, *Science*, 2007, **316**, 1462–5.

5. G. S. Engel, T. R. Calhoun, E. L. Read, T.-K. Ahn, T. Mancal, Y.-C. Cheng, R. E. Blankenship, and G. R. Fleming, *Nature*, 2007, **446**, 782–6.

6. E. Collini, C. Y. Wong, K. E. Wilk, P. M. G. Curmi, P. Brumer, and G. D. Scholes, *Nature*, 2010, **463**, 644–7.

7. I. Kassal, J. Yuen-Zhou, and S. Rahimi-Keshari, *J. Phys. Chem. Lett.*, 2013, **4**, 362–367.

8. J. Huh, S. K. Saikin, J. C. Brookes, S. Valleau, T. Fujita, and A. Aspuru-Guzik, *J. Am. Chem. Soc.*, 2014, **136**, 2048–57.

9. T. Fujita, J. C. Brookes, S. K. Saikin, and A. Aspuru-Guzik, *J. Phys. Chem. Lett.*, 2012, **3**, 2357–2361.

10. G. Panitchayangkoon, D. Hayes, K. A. Fransted, J. R. Caram, E. Harel, J. Wen, R. E. Blankenship, and G. S. Engel, *Proc. Natl. Acad. Sci. U. S. A.*, 2010, **107**, 12766–70.

11. L. Viani, C. Curutchet, and B. Mennucci, *J. Phys. Chem. Lett.*, 2013, **4**, 372–377.

12. C. Olbrich, J. Strümpfer, K. Schulten, and U. Kleinekathöfer, *J. Phys. Chem. B*, 2011, **115**, 758–64.

13. C. Olbrich, J. Strümpfer, K. Schulten, and U. Kleinekathöfer, *J. Phys. Chem. Lett.*, 2011, 1771–1776.

14. A. Kolli, E. J. O'Reilly, G. D. Scholes, and A. Olaya-Castro, *J. Chem. Phys.*, 2012, **137**, 174109.

15. A. Kolli, A. Nazir, and A. Olaya-Castro, *J. Chem. Phys.*, 2011, **135**, 154112.

16. C. Kreisbeck and T. Kramer, *J. Phys. Chem. Lett.*, 2012, **3**, 2828–2833.

17. N. Christensson, H. F. Kauffmann, T. Pullerits, and T. Mančal, *J. Phys. Chem. B*, 2012, **116**, 7449–54.

18. V. Tiwari, W. K. Peters, and D. M. Jonas, *Proc. Natl. Acad. Sci. U. S. A.*, 2013, **110**, 1203–8.

19. A. W. Chin, J. Prior, R. Rosenbach, F. Caycedo-Soler, S. F. Huelga, and M. B. Plenio, *Nat. Phys.*, 2013, **9**, 113–118.

20. J. M. Womick and A. M. Moran, *J. Phys. Chem. B*, 2011, **115**, 1347–56.

21. G. H. Richards, K. E. Wilk, P. M. G. Curmi, H. M. Quiney, and J. A. Davis, *J. Phys. Chem. Lett.*, 2012, **3**, 272–277.

22. D. B. Turner, R. Dinshaw, K.-K. Lee, M. S. Belsley, K. E. Wilk, P. M. G. Curmi, and G. D. Scholes, *Phys. Chem. Chem. Phys.*, 2012, **14**, 4857–74.

23. E. J. O'Reilly and A. Olaya-Castro, *Nat. Commun.*, 2014, **in-print**.

24. J. Pieper, J. Voigt, and G. J. Small, *J. Phys. Chem. B*, 1999, **103**, 2319–2322.

25. E. J. Peterman, van Amerongen H, van Grondelle R, and J. P. Dekker, *Proc. Natl. Acad. Sci. U. S. A.*, 1998, **95**, 6128–33.

26. E. J. G. Peterman, T. Pullerits, R. van Grondelle, and H. van Amerongen, *J. Phys. Chem. B*, 1997, **101**, 4448–4457.

27. R. Jankowiak, M. Reppert, V. Zazubovich, J. Pieper, and T. Reinot, *Chem. Rev.*, 2011, **111**, 4546–98.

28. V. I. Novoderezhkin, A. B. Doust, C. Curutchet, G. D. Scholes, and R. van Grondelle, *Biophys. J.*, 2010, **99**, 344–52.

29. A. Damjanović, I. Kosztin, U. Kleinekathöfer, and K. Schulten, *Phys. Rev. E*, 2002, **65**, 031919.

30. L. Janosi, I. Kosztin, and A. Damjanović, *J. Chem. Phys.*, 2006, **125**, 014903.

31. R. C. Walker, I. P. Mercer, I. R. Gould, and D. R. Klug, *J. Comput. Chem.*, 2007, **28**, 478–90.

32. C. Olbrich and U. Kleinekathöfer, *J. Phys. Chem. B*, 2010, **114**, 12427–37.

33. S. Shim, P. Rebentrost, S. Valleau, and A. Aspuru-Guzik, *Biophys. J.*, 2012, **102**, 649–60.

34. E. Rivera, D. Montemayor, M. Masia, and D. F. Coker, *J. Phys. Chem. B*, 2013, **117**, 5510–21.

35. T. Renger, A. Klinger, F. Steinecker, M. Schmidt am Busch, J. Numata, and F. Müh, *J. Phys. Chem. B*, 2012, **116**, 14565–80.

36. A. B. Doust, I. H. M. van Stokkum, D. S. Larsen, K. E. Wilk, P. M. G. Curmi, R. van Grondelle, and G. D. Scholes, *J. Phys. Chem. B*, 2005, **109**, 14219–26.

37. H. Hossein-Nejad, C. Curutchet, A. Kubica, and G. D. Scholes, *J. Phys. Chem. B*, 2011, **115**, 5243–53.

38. C. Y. Wong, R. M. Alvey, D. B. Turner, K. E. Wilk, D. A. Bryant, P. M. G. Curmi, R. J. Silbey, and G. D. Scholes, *Nat. Chem.*, 2012, **4**, 396–404.

39. A. B. Doust, C. N. J. Marai, S. J. Harrop, K. E. Wilk, P. M. G. Curmi, and G. D. Scholes, *J. Mol. Biol.*, 2004, **344**, 135–53.

40. C. Curutchet, V. I. Novoderezhkin, J. Kongsted, A. Muñoz-Losa, R. van Grondelle, G. D. Scholes, and B. Mennucci, *J. Phys. Chem. B*, 2013, **117**, 4263–73.

41. K. E. Wilk, S. J. Harrop, L. Jankova, D. Edler, G. Keenan, F. Sharples, R. G. Hiller, and P. M. G. Curmi, *Proc. Natl. Acad. Sci.*, 1999, **96**, 8901–8906.

42. A. B. Doust, K. E. Wilk, P. M. G. Curmi, and G. D. Scholes, *J. Photochem. Photobiol. A Chem.*, 2006, **184**, 1–17.

43. C. Curutchet, J. Kongsted, A. Muñoz-Losa, H. Hossein-Nejad, G. D. Scholes, and B. Mennucci, *J. Am. Chem. Soc.*, 2011, **133**, 3078–84.

44. V. May and O. Kühn, *Charge and Energy Transfer Dynamics in Molecular Systems*, Wiley-VCH Verlag GmbH, Weinheim, Germany, 2003.

45. S. Valleau, A. Eisfeld, and A. Aspuru-Guzik, *J. Chem. Phys.*, 2012, **137**, 224103.

46. C. Curutchet, A. Muñoz-Losa, S. Monti, J. Kongsted, G. D. Scholes, and B. Mennucci, *J. Chem. Theory Comput.*, 2009, **5**, 1838–1848.

47. M. C. Zerner, in *Reviews in Computational Chemistry*, eds. K. B. Lipkowitz and D. B. Boyd, Wiley VCH, New York, II., 1994, p. 313.

48. M. Aghtar, J. Strümpfer, C. Olbrich, K. Schulten, and U. Kleinekathöfer, *J. Phys. Chem. B*, 2013, **117**, 7157–63.

49. H. P. Baron R, van Gunsteren WF, *Trends Phys. Chem.*, 2006, **11**, 87.

50. Minnesota Database of Frequency Scale Factors for Electronic Model Chemistries, 2013.

51. L. Viani, *MView: A tool for visualization and analysis of molecular properties. www.mview-tools.com.*

52. V. I. Novoderezhkin and R. van Grondelle, *Phys. Chem. Chem. Phys.*, 2010, **12**, 7352–65.

53. Y. Tanimura and R. Kubo, *J. Phys. Soc. Japan*, 1989, **58**, 101–114.

54. A. Ishizaki and G. R. Fleming, *J. Chem. Phys.*, 2009, **130**, 234111.